

Tunable optical and nano-scale electrical properties of WO_3 and Ag- WO_3 nanocomposite thin films

E. György · A. Pérez del Pino

Received: 27 September 2010/Accepted: 11 January 2011/Published online: 29 January 2011
© Springer Science+Business Media, LLC 2011

Abstract WO_3 and Ag- WO_3 nanocomposite thin films have been synthesized from pure WO_3 and Ag- WO_3 composite pressed powder targets submitted to pulses generated by a frequency quadrupled Nd:yttrium aluminium garnet (YAG; $\lambda = 266 \text{ nm}$, $\tau \sim 5 \text{ ns}$, $v = 10 \text{ Hz}$) laser source. The irradiations were performed in low pressure oxygen atmosphere. The obtained results proved the possibility to tailor the synthesized thin films optical properties in the UV–Visible spectral region and their nano-scale electrical characteristics through the process parameters, as ambient oxygen pressure value during the thin films deposition and Ag concentration of the Ag- WO_3 composite targets. The tunable optical and electrical features allow for the creation of new materials for future applications as photocatalysts, transparent conducting electrodes, electrochromic or chemical and biological sensor devices.

Introduction

Tailoring the functional properties of transition metal oxide and transition metal oxide–noble metal nanocomposite thin

films offer an exciting pathway for the creation of new materials which meet designer-specified optical, electrical, or catalytic properties. Such artificial materials have unique properties and can be employed for various potential applications in areas such as plasmonics, X-ray optics, nonlinear optics, microelectronics and optical data storage.

Among transition-metal oxides, tungsten trioxide (WO_3) attracted the interest of the scientific community due to its promising technological applications. It is a widely used material in electrochromic devices [1–3], selective catalysts for oxidation and reduction reactions [4], as well as transparent conductive oxide electrodes [5]. WO_3 is also of high interest as active layer in NH_3 [6], H_2 [7], H_2S [8], NO_x [9, 10] or CO [11] gas sensors. Inclusion of noble metal nanoparticles (NPs) with high catalytic activity [12] such as Pd, Pt, Ag, Ni or Au in the structure of transition-metal oxides has been reported to be effective for the enhancement of sensitivity and selectivity of gas sensors, reducing the response and recovery times [7, 13–20]. Moreover, photocatalytic activity of noble metal loaded transition metal oxides was improved as compared with bare transition metal oxides. Photocatalytic activity of Ag loaded WO_3 under visible-light irradiation was found to be about three times higher than that of WO_3 [21]. Dispersed Au NPs on TiO_2 films enhanced the photocurrent generation with five folds and the photocatalytic activity was improved more than two folds as compared to TiO_2 under UV light irradiation [22]. Moreover, bactericidal performance of silver modified transition metal oxide photocatalyst was demonstrated. Gram-negative model microorganisms were effectively inactivated by Ag- TiO_2 nanocomposites under visible light irradiation. It was found that the growth of microorganisms can be completely inhibited and thus the nanocomposites are applicable for the removal of biological impurities from drinking and underground water supplies [23, 24].

E. György (✉)
Centre d'Investigacions en Nanociència i Nanotecnologia,
Consejo Superior de Investigaciones Científicas (CIN2-CSIC),
Campus UAB, 08193 Bellaterra, Spain
e-mail: eggyorgy@cin2.es

E. György
National Institute for Lasers, Plasma and Radiations Physics,
P.O. Box MG 36, 77125 Bucharest, Romania

A. Pérez del Pino
Instituto de Ciencia de Materiales de Barcelona, Consejo
Superior de Investigaciones Científicas (ICMAB-CSIC),
Campus UAB, 08193 Bellaterra, Spain

Transition metal oxide–noble metal nanocomposite thin films and nanostructures have been fabricated by many different processing methods including sol–gel procedures [25], DC and RF magnetron sputtering [26, 27], direct femtosecond laser irradiation and successive annealing [28], or pulsed laser deposition (PLD) [29–31]. PLD has numerous advantages over other, classical, deposition methods. It permits a good control of both the crystalline state of the synthesized materials and their adherence to the substrate surface. Moreover, since the energy source is outside the enclosure where the synthesis process takes place, the incorporation of contaminants in the growing films during the deposition process is avoided [32–34].

The authors present results on the characterization of WO_3 thin films and Ag– WO_3 nanocomposite thin films grown by pulsed laser deposition (PLD) technique on SiO_2 (001) quartz substrates. A frequency quadrupled Nd:YAG laser was used for the irradiations. The experiments were performed in controlled oxygen atmosphere. This study is a continuation of the study concerning WO_3 thin films synthesis by pulsed laser deposition [35]. The previous results served as starting point for the setting of the process parameters. It was found that oxygen pressure higher than 10 Pa lead to the synthesis of oxide thin films, below this value the films were metallic. In this article the authors investigated (i) the effect of the ambient oxygen pressure value above this threshold value and (ii) the Ag dopant concentration in the Ag– WO_3 composite targets submitted to laser irradiation on the surface morphology, composition, crystalline status of the synthesised WO_3 thin films as well as Ag– WO_3 nanocomposite thin films. The obtained results were correlated with the films' functional, optical and nano-scale electrical properties.

Experimental details

The growth of WO_3 and Ag– WO_3 nanocomposite thin films was performed inside a stainless steel reaction chamber. A pulsed frequency quadrupled Nd:YAG laser ($\lambda = 266$ nm, $\tau_{\text{FWHM}} \sim 5$ ns, $v = 10$ Hz) was used as energy source. The laser fluence on the surface of the WO_3 and Ag– WO_3 composite targets was fixed at 3 J/cm^2 . The laser beam incidence angle was about 45° relative to the normal of the targets surface. The target preparation protocol consisted of pressing of WO_3 and mixture of Ag and WO_3 powders at 0.5 MPa pressure. The Ag concentration was chosen in the (1.5–3) wt% range. The obtained pellets were sintered for 6 h at 1100°C temperature.

The targets were translated and simultaneously rotated during the multipulse laser irradiation with a frequency of 3 Hz. The SiO_2 (001) quartz substrates were positioned at 30 mm separation distance from the target surface, parallel

to it. Before the laser irradiation experiments the targets and substrates were carefully cleaned with acetone in ultrasonic bath. Additional target cleaning was performed by a preliminary ablation step which proved to be essential for removing the last contaminants and impurities. During this process a shutter was interposed between the targets and the substrate, parallel to them. Prior to each irradiation the vacuum chamber was evacuated down to a residual pressure of 10^{-4} Pa. High purity oxygen (99.9%) was then circulated inside the irradiation chamber through a calibrated gas inlet. The dynamic oxygen pressure was maintained constant during the thin films synthesis process at 10 or 20 Pa.

To avoid film peeling and/or cracking the authors used an EUROTERM controller device which allows for substrate heating and cooling with a smooth ramp. During the film growth the substrate temperature was fixed at 600°C . Once the growth process was completed, the films were cooled down with a ramp of $10^\circ\text{C}/\text{min}$. maintaining the oxygen pressure identical to that used during the deposition experiments. 15,000 subsequent laser pulses were applied for the growth of each film.

The WO_3 as well as Ag– WO_3 nanocomposite thin films were studied by atomic force microscopy (AFM) with a PicoSPM Molecular Imaging apparatus. The films surface morphology was studied by acoustic (dynamic) mode while their local electric properties by current sensing AFM (CSAFM) [36, 37]. The crystalline status of the films was investigated by selected area electron diffraction (SAED) with a JEOL 1210 transmission electron microscope (TEM) operated at 200 keV and X-ray diffraction (XRD) in θ – 2θ configuration with a Philips MRD diffractometer ($\text{CuK}\alpha$, $\lambda = 1.5418 \text{ \AA}$ radiation). The preparation of the samples for TEM studies was carried out by the extraction replica method. The optical absorbance and transmittance measurements were performed with a double beam Perkin Elmer Lambda 19 spectrophotometer in the wavelength range of (300–1000) nm.

Results and discussion

Morphological and structural properties

Figure 1 shows the AFM images, surface profiles and local height histograms counted on $1.0 \times 1.0 \mu\text{m}^2$ surface areas of WO_3 and Ag– WO_3 thin films deposited at 10 Pa oxygen pressure. The surface local height histograms can be approximated by a simple Gaussian distribution. The WO_3 film shows grain-like features, with a root mean square (RMS) surface roughness of about 4 nm. The average surface local height and the in-plane diameters of the grains remain approximately the same with the increase of the

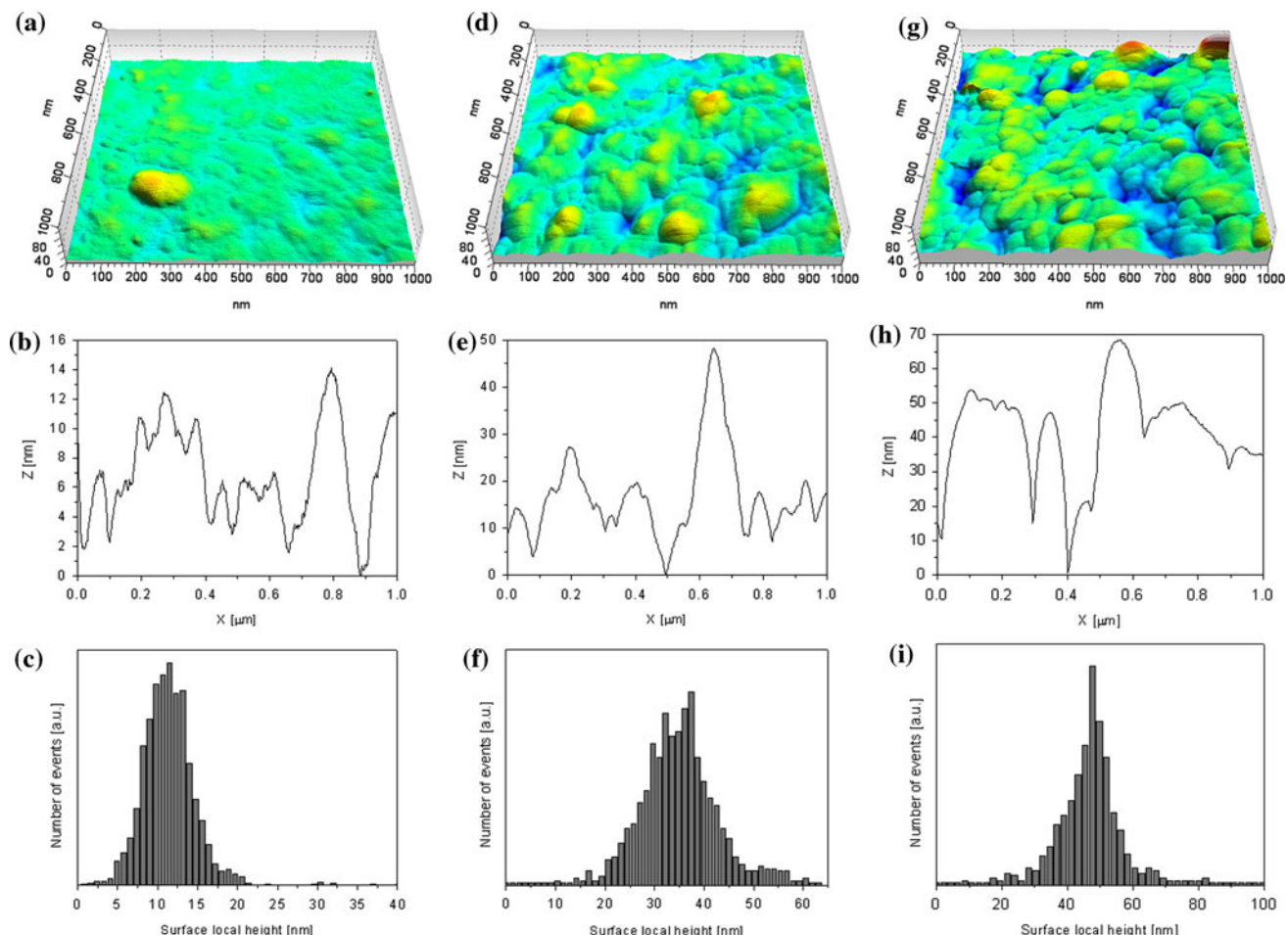


Fig. 1 AFM images, surface profiles, and histograms of surface local heights of (**a, b, c**) WO_3 thin film as well as Ag- WO_3 nanocomposite thin films obtained through the irradiation of (**d, e, f**) 1.5 and (**g, h, i**) 3 wt% Ag concentration WO_3 targets at 10 Pa oxygen pressure

ambient oxygen pressure from 10 to 20 Pa. The surface morphologies of the Ag- WO_3 films are completely different, consisting mostly of large agglomerates. Both in-plane diameters and height of the surface agglomerates increase with the increase of the dopant concentration from 1.5 (Fig. 1d-f) to 3 wt% (Fig. 1g-i). The RMS roughness of the films obtained from the 1.5 and 3 wt% Ag- WO_3 composite targets is 8 and 10 nm, respectively.

The bright field TEM investigations (Fig. 2a) evidenced that the thin films are composed by nanoparticles with average dimensions around 15 nm. Fig. 2b and c show the two different, characteristic SAED patterns corresponding to selected zones of the sample deposited at 10 Pa oxygen pressure and 3 wt% Ag-doping concentration of the composite target. Indexing the SAED pattern in Fig. 2b the authors obtain interplanar distances of 0.385 and 0.192 nm assigned to the (001) and (002) lattice plane reflections of the orthorhombic β - WO_3 phase, with lattice parameters $a = 7.38$, $b = 7.51$ and $c = 3.84 \text{ \AA}$, as referred in the

JCPDS 20–1324 file [38]. According to the phase diagram, WO_3 adopts at least five different crystallographic phases at temperatures between zero and its melting point. The phase transition occurs in sequence in the order monoclinic ε - WO_3 , triclinic δ - WO_3 , monoclinic γ - WO_3 , orthorhombic β - WO_3 and tetragonal α - WO_3 . The monoclinic γ - WO_3 to orthorhombic β - WO_3 phase transformation, in bulk, takes place above 320 °C [39]. The SAED pattern in Fig. 2c shows interplanar distances of 0.235, 0.144 and 0.117 nm attributed to the (111), (222) and (220) lattice plane reflections of the polycrystalline cubic Ag phase as referred in the JCPDS 04-0783 file [38]. As can be observed, the diffraction rings are discontinuous, constituted by sharp spots, indicating that the WO_3 matrix and Ag nanoparticles are well crystallized. No signal from Ag oxide is observed.

In order to obtain a more general view on the crystalline structure, the synthesized thin films were also investigated by XRD (Fig. 3). The diffractograms of the films deposited at 10 and 20 Pa oxygen pressure are composed by the same

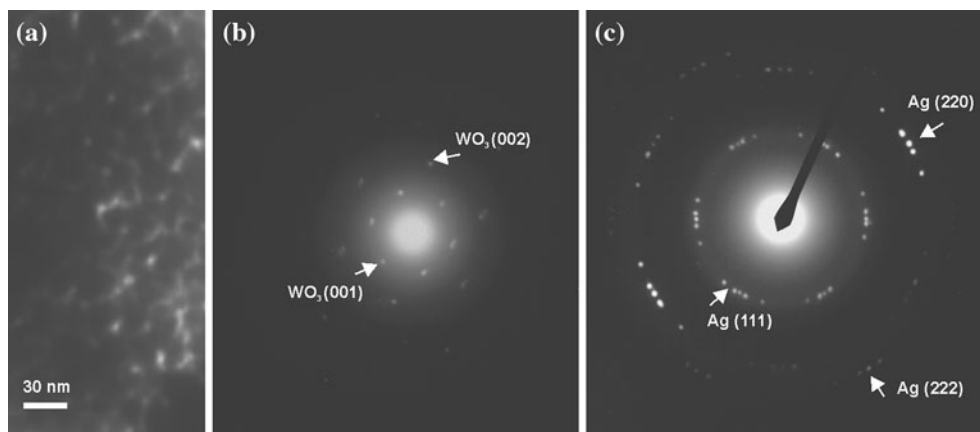


Fig. 2 **a** TEM micrograph and **b, c** SAED patterns of Ag-WO₃ nanocomposite thin film obtained through the irradiation of 3 wt% Ag concentration WO₃ targets at 10 Pa oxygen pressure

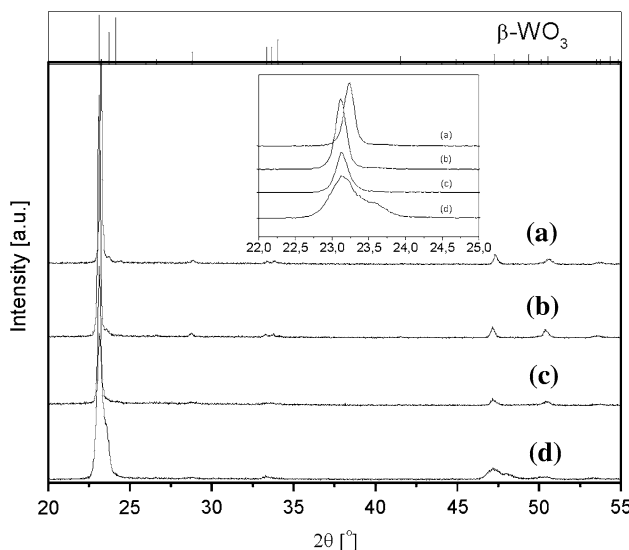


Fig. 3 X-ray diffractograms of WO₃ thin films deposited at **a** 20 and **b** 10 Pa oxygen pressure as well as Ag-WO₃ nanocomposite thin films obtained through the irradiation of **c** 1.5 and **d** 3 wt% Ag concentration WO₃ targets at 10 Pa oxygen pressure

main diffraction lines at 23.1°, 47.2° and 50.4° attributed to the (001), (002) and (112) lattice plane reflections of the orthorhombic β -WO₃ phase indicating a strong preferred orientation along the [001] crystal direction, i.e., a mechanism of film growth with the crystallographic axis c perpendicular to the substrate surface, in accordance with the SAED results. Nevertheless, with the increase of the Ag concentration, the intensity of the 23.1° line corresponding to the (001) lattice plane reflection decreases gradually, while its full width at half maximum increases (see inserts of Fig. 3) indicating that crystallization was inhibited by metal additives incorporation. Metal additives are well known to modify the oxides grain growth kinetics [40–43]. The grain growth retard was attributed to localized additive

concentration [40]. Moreover, at the highest, 3 wt% dopant concentration an additional line, at 23.6° appear attributed to the (020) lattice plane reflection of the orthorhombic β -WO₃ phase. A shift of about 0.2° of the line corresponding to the (001) lattice plane reflection towards higher values with the increase of the ambient oxygen pressure can be also observed in the insert. Similar shift of the (001) lattice plane towards lower diffraction angles with the increase of the oxygen pressure was observed also in case of LaTiO₃ thin films grown by PLD, under similar experimental conditions, due to the change of the lattice d-spacing parallel to the substrate surface [44].

No lines corresponding to the lattice plane reflections of the polycrystalline cubic phase Ag are present in the diffraction patterns. This is due the most probably to the low fraction of Ag nanometer sized clusters in the films. The authors would like to note that a film thickness of about 150 nm was measured by surface profilometry. For the 3 wt% Ag-doping concentration it can be estimated an equivalent Ag thickness of several nm. To check the hypothesis, Ag thin films were deposited under identical experimental conditions from metallic Ag substituting the Ag doped WO₃ composite targets. Ag diffraction lines can be identified by XRD measurements performed under the present configuration only for thickness values of tens of nm.

The average size of nanocrystallites in the films was determined by the Scherrer equation [45]: $D_{hkl} = 0.9\lambda/\beta_{hkl}\cos\theta_{hkl}$ where λ is the X-ray wavelength, θ_{hkl} is the Bragg diffraction angle, and β_{hkl} is the full width at half-maximum (FWHM) in radian of the diffraction line corresponding to the (001) lattice plane reflection. The obtained results are summarized in Table 1. As can be observed, the nanocrystallites size does not change with the ambient gas pressure. However, the dopant incorporation leads to the decrease of the crystallites average dimensions.

Table 1 WO_3 nanocrystallites average size, calculated from the X-ray diffraction data using the Scherrer equation and Urbach energy as a function of ambient gas pressure and Ag concentration

Oxygen pressure (Pa)	Ag concentration (wt%)	Nanocrystallites size (nm)	Urbach energy (meV)
20	0	32.5	294
10	0	32.5	360
10	1.5	27.0	400
10	3.0	16.2	420

These results, i.e., inhibition of crystallization with dopant incorporation are in good concordance with other studies concerning doped transition metal oxide thin films. Crystallization during the growth process has been demonstrated to be strongly hindered by the presence of dopant materials as Au, Pd and Pt in SnO_2 [40, 41], Pt in TiO_2 [42] and Ag in ZnO [43] films. The effect has been attributed to the incorporation of the dopant into the crystal lattice in both interstitial and substitutional sites.

Optical and electrical properties

The transmittance spectra in the UV–Visible spectral ranges of the WO_3 and Ag– WO_3 thin films are shown in Fig. 4I. The spectrum corresponding to the SiO_2 (001) quartz substrates is also presented. Subtracting the spectrum of the substrate, the average transmittance of the WO_3 film deposited at high, 20 Pa, oxygen pressure is found to be close to 90% in the visible spectral range. Conversely, the average transmittance in the visible spectral range of the WO_3 film deposited at 10 Pa is very low, less than 40% at 500 nm and then gradually decreases in the higher wavelength region. With the increase of the Ag concentration the average transmittance further decreases up to a value of less than 20%.

From the optical transmittance spectra the chromaticity coordinates (x, y) and the standard tristimulus value, Y , of the thin films were calculated. As known, the chromaticity coordinates specify the colour in the CIE chromaticity

Table 2 Chromaticity coordinates, (x, y), and tristimulus, Y , value of the obtained WO_3 and Ag– WO_3 nanocomposite thin films as a function of ambient gas pressure and Ag concentration

Oxygen pressure (Pa)	Ag concentration (wt%)	(x, y)	Y	Colour
20	0	(0.35, 0.34)	807	Transparent
10	0	(0.29, 0.32)	341	Blue-transparent
10	1.5	(0.16, 0.12)	16	Blue-translucent
10	3.0	(0.16, 0.1)	8	Dark blue-translucent

diagram, while the standard tristimulus value is a measure of the brightness [46]. Table 2 contains the obtained results. The authors attributed the low transmittance values at low oxygen pressure to the formation of oxygen vacancies, i.e., sub-stoichiometric WO_{3-y} films. Indeed, the films deposited at 10 and 20 Pa exhibit also different chromatic properties. They are dark blue at 10 Pa and completely transparent at 20 Pa. It was reported that dark blue colour is attributed to oxygen deficient metallic films with $y \sim 0.3\text{--}0.5$, while in case of $y < 0.3$ the films are transparent and resistive [47]. This suggests a partial decomposition of the WO_3 compound target material irradiated by the subsequent laser pulses. The evaporated species are re-oxidised during their transit towards the substrate's surface, low, 10 Pa, oxygen pressure leading only to partial re-oxidation. Similar results were found also in case of films deposited by r.f. sputtering in low oxygen pressure [48]. Furthermore, oxygen vacancies were reported to red shift the absorption edge, accompanied by increase of absorption at wavelengths >600 nm, corroborating well with these results (Fig. 4II a, b) [49].

The optical absorption of the Ag– WO_3 samples increases in the visible spectral region with the increase of the Ag concentration. This behaviour can be attributed to the surface plasmon resonance (SPR) absorption, characteristic to the metallic Ag nanoparticles [50]. The shift of the absorption maximum towards higher wavelengths with the increase of the dopant concentration and peak broadening could be due to the increase in the in-plane diameter

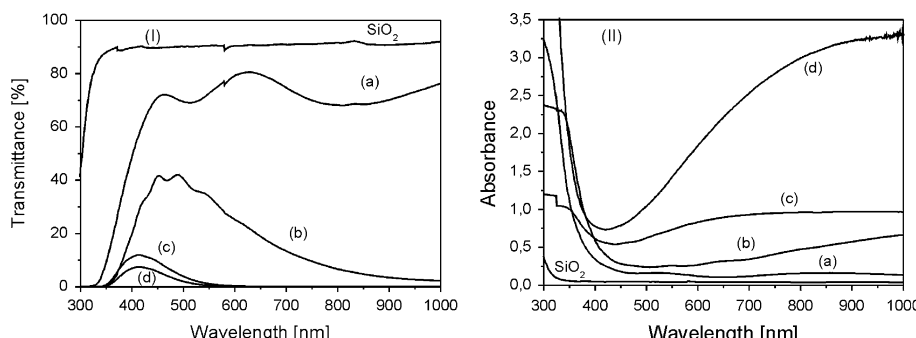
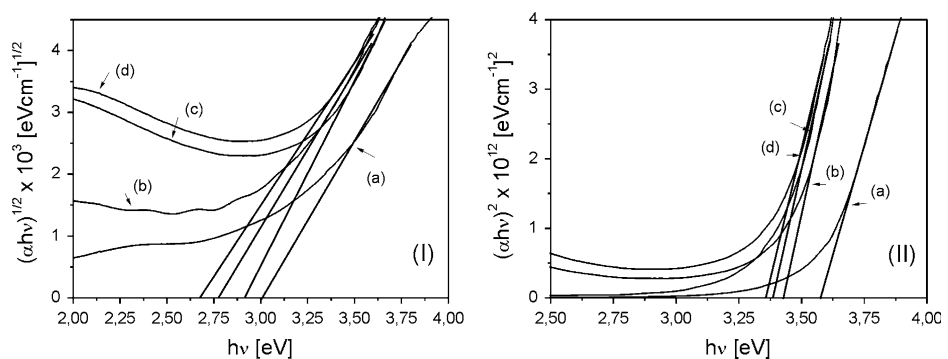
Fig. 4 Transmittance (I) and absorbance (II) spectra of WO_3 thin films deposited at **a** 20 and **b** 10 Pa oxygen pressure as well as Ag– WO_3 nanocomposite thin films obtained through the irradiation of **c** 1.5 and **d** 3 wt% Ag concentration WO_3 targets at 10 Pa oxygen pressure

Fig. 5 $(\alpha h\nu)^{1/2}$ (I) and $(\alpha h\nu)^2$ (II) versus $h\nu$ curves corresponding to WO_3 thin films deposited at **a** 20 and **b** 10 Pa oxygen pressure as well as Ag- WO_3 nanocomposite thin films obtained through the irradiation of **c** 1.5 and **d** 3 wt% Ag concentration WO_3 targets at 10 Pa oxygen pressure



[51, 52] and/or aggregation of nanoparticles [53]. Red shift of SPR peak from 425 to 737 nm was reported for laser deposited Ag nanoparticles as the particles diameter increases from 7.1 to 72.3 nm [54]. On the other hand, SPR peak positions below 410 nm were observed for very small, less than 5 nm Ag nanoparticles, the particles mean size being estimated both from direct measurements and calculated [55].

The optical absorption coefficient, α , was calculated from the expression $\alpha = A \ln(10)/d$, where A stands for the absorbance and d for the thickness of the films [56]. From surface profilometry data the thickness of the films was evaluated to be around 150 nm. The authors estimated the optical band gap, E_g , using the Tauc plot, from the extrapolation of the linear part of the $(\alpha h\nu)^{1/m}$ versus $h\nu$ curves, where $h\nu$ is the incident photon energy [57]. As known, above the fundamental absorption threshold the absorption coefficient follows the relation $\alpha h\nu \sim (h\nu - E_g)^m$, where $m = 2$ for the indirect and $1/2$ for directly allowed transitions. To determine the possible transitions $(\alpha h\nu)^{1/m}$ versus $h\nu$ were plotted both for $m = 2$ and $1/2$ (Fig. 5), being the $(\alpha h\nu)^2$ versus $h\nu$ plot which covers the widest range of data points corresponding to the directly allowed transition.

From the $(\alpha h\nu)^2$ versus $h\nu$ plots the direct band gap values can be estimated. The band gap value of the reference film deposited at 20 Pa oxygen pressure was estimated at around 3.6 eV, slightly exceeding the value of bulk material of 3.5 eV. The band gap broadening could be attributed to the well known quantum confinement effect in the nanocrystalline thin films [58]. Band gap narrowing can be observed for WO_3 films with the decrease of the oxygen pressure, assigned to the formation of oxygen deficient sub-stoichiometric WO_{3-y} . Indeed, band structure calculations of tungsten oxide thin films reveal that oxygen deficiency is correlated with the formation of deep localised states in the band gap [59]. Further systematic band gap narrowing was observed with the increase of the dopant concentration. Until a certain extent similar band gap narrowing was observed for $\text{ZnO}/\text{Ag}/\text{ZnO}$ multilayers with Ag layer thickness in the range 8–14 nm [60]. The optical band gap

of multilayer films was found to decrease with increasing the thickness of the Ag layer. The change of the band gap was attributed to charge transfer from Ag to ZnO layer causing downward shifting of the conduction band and upward shifting of the valence band.

At photon energy values below the absorption edge it is noteworthy to evaluate the Urbach energy (Urbach tail) in case of semiconductor films. It is known that structural disorders generate band tails of localised states [61–64]. Urbach energy, E_0 , estimated from the expression $\alpha(h\nu) = \alpha_0 \exp(h\nu/E_0)$ [65], is the inverse of the slope of the linear fit to the logarithmic plot of the absorption coefficient (Table 1). The value calculated for the WO_3 thin film deposited at 20 Pa oxygen pressure is similar to that reported in literature for undoped WO_3 thin films grown by pulsed laser deposition [61]. The dependence of the Urbach energy on oxygen pressure and Ag concentration supports that formation of oxygen vacancies as well as Ag incorporation introduce lattice disorder in the oxide matrix.

In order to investigate the local conductivity on the WO_3 and Ag- WO_3 thin films the authors recorded the current–voltage (I – V) characteristic curves in different surface areas through CSAFM technique, using biased Pt–Ir coated silicon tips in contact mode. The I – V curves of the WO_3 thin films (Fig. 6a) show a non-ohmic behaviour. This feature could be attributed to the semiconducting properties of the WO_3 films. The turn-on voltage value ranges between 0.1 and 0.3 V and the resistance at 0 V is around 0.4–2.5 G Ω , depending on the surface location. Typical curves, corresponding to the thin films obtained from the Ag- WO_3 composite targets confirms the presence of metallic Ag clusters on the films surface (dashed lines in Fig. 6b) showing a nearly ohmic behaviour. No remarkable differences can be discerned between the I – V curves of the samples obtained from 1.5 and 3 wt% Ag- WO_3 targets. The calculated resistance values at 0 V are smaller, around 0.03–0.1 G Ω , as compared to WO_3 surface locations, which show similar values to those measured for the WO_3 films (see Fig. 6a and scattered plots in Fig. 6b). The slight deviation from the linearity could be due to the contribution of the semiconducting WO_3 or the size dispersion of

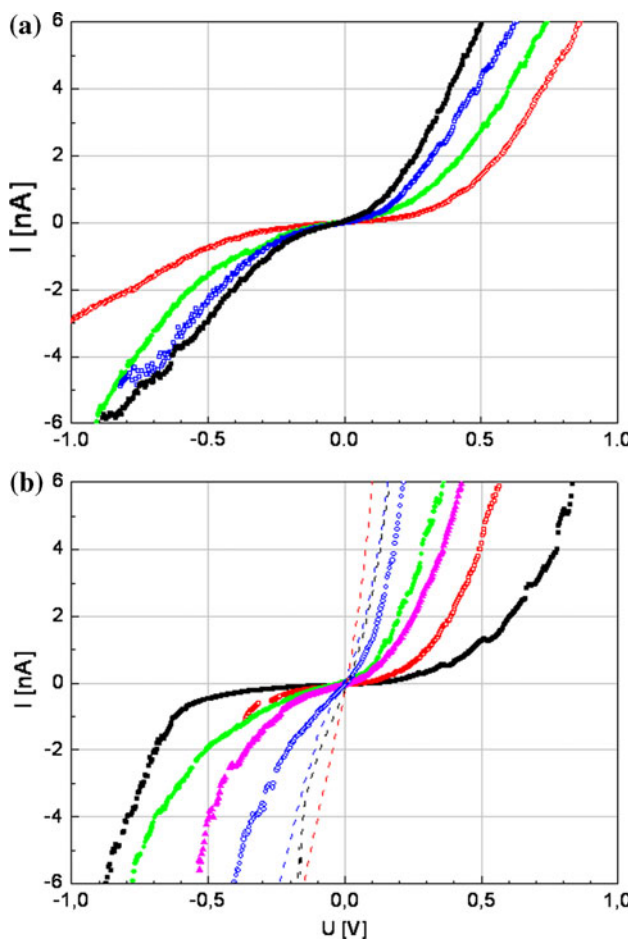


Fig. 6 Typical I - V characteristics of **a** WO_3 thin film and **b** $\text{Ag}-\text{WO}_3$ nanocomposite thin film obtained through the irradiation of 3 wt% Ag concentration WO_3 targets, both deposited at 10 Pa oxygen pressure

the Ag particles. Studies of local electric properties performed for Au clusters deposited on MgO and TiO_2 surfaces [66, 67], point to distinct I - V curves depending on the cluster size. The gradual transition from insulator up to the bulk metallic electronic structure proceeds along with the increase of the metal cluster sizes, and the metallic behaviour becomes obvious for clusters with diameters larger than about 5 nm. The authors recall that in sensor applications the presence of metallic clusters is required to ensure better selectivity and sensitivity, as well as diminishment of the response time and working temperature as compared to the base, uncovered transition metal oxide [66–69].

Conclusions

WO_3 as well as $\text{Ag}-\text{WO}_3$ nanocomposite thin films were grown on SiO_2 (001) quartz substrates by pulsed laser deposition using a frequency quadrupled Nd:YAG laser

source. The effect of the ambient oxygen pressure and Ag concentration on the surface morphology, crystalline status, and optical properties of the films was investigated. The gradual band gap narrowing and change of the average optical absorption in the visible spectral region were attributed to the films chemical composition, i.e., oxygen stoichiometry and Ag incorporation, both controlled by the deposition parameters. The I - V characteristics indicate the growth of WO_3 thin films with non-ohmic behaviour. The local, nano-scale electric measurements confirm the presence of metallic Ag clusters on the films surface. The accordable optical and electrical features allow for the design of new composite materials for applications as transparent conducting electrodes, active layers in chemical or biological sensors, photocatalytic as well as electrochromic devices.

Acknowledgements Financial support from the Ministry of Science and Innovation of the Spanish Government under the projects MAT2008-04931 and CSD2008-00023 is acknowledged with thanks.

References

1. Granqvist CG (1995) Handbook on inorganic electrochromic materials. Elsevier Science, Amsterdam
2. Deepa M, Sharma R, Basu A, Agnihotry SA (2005) *Electrochim Acta* 50:3545
3. Balaji S, Djaoued Y, Albert AS, Ferguson RZ, Brüning R, Su BL (2009) *J Mater Sci* 44:6608. doi:[10.1007/s10853-009-3575-8](https://doi.org/10.1007/s10853-009-3575-8)
4. Cotton FA, Wilkinson G (1988) Advanced organic chemistry, 5th edn. Wiley, New York, p 829
5. Stierna B, Granqvist CG (1991) *Appl Opt* 29:117
6. Xu CN, Miura N, Ishida Y, Matsuda K, Yamazoe N (2000) *Sens Actuators B* 65:163
7. Ippolito SJ, Kandasamy S, Kalantar-Zadeh K, Włodarski W (2005) *Sens Actuators B* 108:154
8. Barrett EPS, Georgiades GC, Sermon PA (1990) *Sens Actuators B* 1:116
9. Cantalini C, Sun HT, Faccio M, Pelino M, Santucci S, Lozzi L, Passacantando M (1996) *Sens Actuators B* 31:81
10. Prasad AK, Gouma PI (2003) *J Mater Sci* 38:4347. doi:[10.1023/A:1026339216910](https://doi.org/10.1023/A:1026339216910)
11. Gopel W, Schierbaum KD (1995) *Sens Actuators B* 26–27:1
12. Carabineiro SAC, Bogdanchikova N, -Borja MA, Pestyakov A, Tavares PB, Figueiredo JL (2010) *Nano Res*. doi: [10.1007/s12274-010-0068-7](https://doi.org/10.1007/s12274-010-0068-7)
13. Penza M, Martucci C, Cassano G (1998) *Sens Actuators B* 50:52
14. Tao WH, Tsai CH (2002) *Sens Actuators B* 81:237
15. LeGore LJ, Lad RJ, Vettelino JF, Frederick BG, Kenik EA (2001) *Sens Actuators B* 76:373
16. Ando M, Chabivkovsky R, Haruta M (2001) *Sens Actuators B* 76:13
17. Chen L, Tsang SC (2003) *Sens Actuators B* 89:68
18. Park CO, Akbar SA (2003) *J Mater Sci* 38:4611. doi:[10.1023/A:1027402430153](https://doi.org/10.1023/A:1027402430153)
19. Chaudhari GN, Bambole DR, Bodade AB, Padole PR (2006) *J Mater Sci* 41:4860. doi:[10.1007/s10853-006-0042-7](https://doi.org/10.1007/s10853-006-0042-7)
20. Wang C, Yin L, Zhang L, Xiang D, Gao R (2010) *Sensors* 10: 2088

21. Sun SM, Wang WZ, Zeng SZ, Shang M, Zhang L (2010) *J Hazard Mater* 178:427
22. Fu PF, Zhang PY (2010) *Appl Catal B Env* 96:176
23. Pan XB, Medina-Ramirez M, Mernaugh R, Liu JB (2010) *Colloids Surf B Biointerfaces* 77:82
24. Chen SF, Li JP, Qian K, Xu WP, Lu Y, Huang WX, Yu SH (2010) *Nano Res* 3:244
25. Taurino A, Catalano M, Rella R, Siciliano P, Wlodarski W (2003) *J Appl Phys* 93:3816
26. Tseng IH, Wu JCS, Chou HY (2004) *J Catal* 221:432
27. Subrahmanyam A, Barik UK (2006) *J Phys Chem Solids* 67:1518
28. Ryu SW, Kim EJ, Ko SK, Hahn SH (2004) *Mater Lett* 58:582
29. Zhao QZ, Qiu JR, Jiang XW, Zhao CJ, Zhu CS (2004) *J Appl Phys* 96:7122
30. György E, Sauthier G, Figueras A, Giannoudakos A, Komitsas M, Mihailescu IN (2006) *J Appl Phys* 100:114302
31. Serna R, Gonzalo J, Suarez-Garcia A, Afonso CN, Babonneau D (2006) *Nanotechnology* 17:4588
32. Murakami K (1992) In: Fogarassy E, Lazare S (eds) *Laser ablation of electronic materials – basic mechanisms and applications*. Elsevier, Amsterdam, p 125
33. Bäuerle D (1996) *Laser processing and chemistry*. Springer-Verlag, Berlin
34. Chrisey DG, Hubler GK (eds) (1994) *Pulsed laser deposition of thin films*. Wiley, New York
35. György E, Socol G, Mihailescu IN, Ducu C, Ciucă S (2005) *J Appl Phys* 97:093527
36. Schneegans O, Houzé F, Meyer R, Boyer L (1998) *IEEE Trans Comp Packaging Manufact Technol Part A* 21:76
37. Iseri Y, Honda M, Kim YD, Ando T, Choi W, Tomokage H (2004) *J Phys Condens Matter* 16:S171
38. Powder Diffraction File (1986) JCPDS International Centre for Diffraction Data Pennsylvania, USA
39. Granqvist CG (1995) *Handbook of inorganic electrochromic materials*. Elsevier, Amsterdam
40. Cabot A, Diéguez A, Romano-Rodríguez A, Morante JR, Barsan N (2001) *Sensors Actuators B* 79:98
41. Miller TA, Bakrania SD, Perez C, Wooldridge MS (2005) *J Mater Res* 20:2977
42. György E, Axente E, Mihailescu IN, Ducu C, Du H (2006) *Appl Surf Sci* 252:4578
43. Georgekutty R, Seery MK, Pillai SC (2008) *J Phys Chem C* 122:13563
44. Kim KH, Norton DP, Budai JD, Chisholm MF, Sales BC, Christen DK, Cantoni C (2003) *Phs Stat Sol* 200:346
45. Cullity DB (1978) *Elements of X-ray diffraction*. Addison Wesley, Reading
46. Guild J (1931) *Phil Trans R Soc A* 230:149
47. Zhang JG, Benson DK, Tracy CE, Deb SK, Czanderna AW (1997) *J Electrochem Soc* 144:2022
48. Prabakar K, Takahashi T, Takahashi K, Nezuka T, Nakashima T, Kubota Y, Fujishima A (2007) *J Vac Sci Technol A* 25:1029
49. Lin Z, Orlov A, Lambert RM, Payne MC (2005) *J Phys Chem* 109:20948
50. Kreibig U, Vollmer M (1995) *Optical properties of metal clusters*. Springer, Berlin
51. Lim SK, Chung KJ, Kim CK, Shin DW, Kim YH, Yoon CS (2005) *J Appl Phys* 98:084309
52. Schaadt DM, Feng B, Yu ET (2005) *Appl Phys Lett* 86:063106
53. Bhui DK, Bar H, Sarkar P, Sahoo GP, De SP, Misra A (2009) *J Molec Liquids* 145:33
54. Alonso JC, Diamant R, Castillo P, Acosta-Garcia MC, Batina N, Haro-Poniatowski E (2009) *Appl Surf Sci* 255:4933
55. Pan A, Yang Z, Zheng H, Liu F, Zhu Y, Su X, Ding Z (2003) *Appl Surf Sci* 205:323
56. Pankove JI (1971) *Optical processes in semiconductors*. Prentice-Hall, Englewood Cliffs
57. Tauc J, Grigorovici R, Vancu A (1966) *Phys Status Solidi* 15:627
58. Barykin DV, Friedrich JM, Walsh FC (2006) *Adv Mater* 18:2807
59. de Wijs GA, De Groot RA (2001) *Electrochim Acta* 46:1989
60. Han H, Theodore ND, Alford TL (2008) *J Appl Phys* 103:013708
61. Lethy KJ, Beena D, Pillai VPM, Ganesan V (2008) *J Appl Phys* 104:033515
62. Chen NB, Wu HZ, Qiu DJ, Xu TN, Chen J, Shen WZ (2004) *J Phys Condens Matter* 16:2973
63. Anwar M, Ghauri IM, Siddiqi SA (2006) *J Mater Sci* 41:2859. doi:[10.1007/s10853-005-5158-7](https://doi.org/10.1007/s10853-005-5158-7)
64. Yang J, Gao YQ, Wu J, Huang ZM, Meng XJ, Shen MR, Sun JL, Chu JH (2010) *J Appl Phys* 108:114102
65. Grundmann M (2006) *The physics of semiconductors*. Springer-Verlag, Berlin
66. Xu C, Oh WS, Liu G, Kim DY, Goodman DW (1997) *J Vac Sci Technol* 15:1261
67. Freund HJ (2002) *Surf Sci* 500:271
68. Campbell CT (1997) *Surf Sci Rep* 27:111
69. Chen DA, Bartelt MC, Hwang RQ, McCarty KF (2000) *Surf Sci* 450:78